Available online at www.sciencedirect.com
ScienceDirect
Acta Biomaterialia 5 (2009) 743–754
Acta BIOMATERIALIA
www.elsevier.com/locate/actabiomat

Electrical characterization of hydroxyapatite-based bioceramics

J.P. Gittings [a], C.R. Bowen [a,*], A.C.E. Dent [a], I.G. Turner [a], F.R. Baxter [a,b], J.B. Chaudhuri [b]

[a] *Materials Research Centre, Department of Mechanical Engineering, University of Bath, Claverton Down, Bath BA2 7AY, UK*
[b] *Department of Chemical Engineering, University of Bath, Bath BA2 7AY, UK*

Received 20 February 2008; received in revised form 30 June 2008; accepted 12 August 2008
Available online 5 September 2008

Abstract

This paper studies the AC conductivity and permittivity of hydroxyapatite (HA)-based ceramics from 0.1 Hz–1 MHz at temperatures from room temperature to 1000 °C. HA-based ceramics were prepared either as dense ceramics or in porous form with interconnected porosity and were sintered in either air or water vapour. Samples were thermally cycled to examine the influence of water desorption on AC conductivity and permittivity. Surface-bound water was thought to contribute to conductivity for both dense and porous materials at temperatures below 200 °C. At temperatures below 700 °C the permittivity and AC conductivity of HA was also influenced by the degree of dehydration and thermal history. At higher temperatures (700–1000 °C), bulk ionic conduction was dominant and activation energies were of the order of ~2 eV, indicating that hydroxyl ions are responsible for conductivity.

Keywords: Hydroxyapatite; Dielectric; Sintering; Polarization; Bioceramics

1. Introduction

Hydroxyapatite (HA), $Ca_{10}(PO_4)_6(OH)_2$, has the ability to chemically interact with bone both in vitro and in vivo [1]. For this reason it has been extensively researched as a possible bone substitute material [1–4]. While a significant amount of research on HA has concentrated on its mechanical properties and biocompatibility [2–6], there has also been interest in the electrical properties of the material [7–20]. HA has a lattice of hydroxyl ions (OH^-) located at the centre of Ca^{2+} triangles along the *c*-axis of a hexagonal unit cell [7]. The OH^- ions are aligned in columns parallel to the *c*-axis, along with Ca^{2+} and (PO_4^{3-}) ions [8]. Since the OH^- ions within the *c*-axis columns are thought to have an important role in ionic conduction [7], HA has been regarded as a one-dimensional anionic conductor [9].

The study of the DC and AC electrical properties of HA has been of interest for a variety of reasons. Hoepfner and Case [10] reported the influence of porosity on the room temperature permittivity of HA to understand its interaction with electrical fields applied to improve fracture healing or enhance bone growth. The concept of implant electrical stimulation prompted Zakharov et al. to examine the temperature dependence of permittivity and dielectric loss of HA at temperatures between 20 and 500 °C [11,12]. Nagai and Nishino [13] examined the surface ionic conduction of porous and dense HA for humidity sensor applications, since the room temperature conductivity was influenced by relative humidity. The ionic conductivity of HA has been a subject of research for its possible use as an alcohol [9], carbon dioxide [9] or carbon monoxide gas sensor [8]. Electrical measurements have also been used as a characterization tool to study the evolution of microstructure in HA [14] and study composites [15] such as HA–ZrO_2 [16] and HA–Ti [17]. Valdes et al. [18] examined the dielectric properties of HA to understand its decomposition to tri-calcium phosphate (TCP; $Ca_3(PO_4)_2$) as a result of the dehydration of OH^- ions at elevated temperatures [19]. This was of interest since TCP was thought to have higher bioactivity than HA. The dielectric properties of thin films of HA have also been measured at room temperature [20,21].

* Corresponding author. Tel.: +44 1225 383660.
E-mail address: c.r.bowen@bath.ac.uk (C.R. Bowen).

1742-7061/$ - see front matter © 2008 Acta Materialia Inc. Published by Elsevier Ltd. All rights reserved.
doi:10.1016/j.actbio.2008.08.012

There has also been recent interest in the polarization of HA to generate a surface charge by the application of electric fields (kV cm^{-1}) at elevated temperature (>200 °C). The presence of surface charges on HA has been shown to have a significant effect on the crystallization of inorganic ions dissolved in vitro or in vivo [22–25]. Bone growth was accelerated on negatively charged surfaces and decelerated at positively charged surfaces [26], and Nakamura et al. [27] recently reported that both positive and negative charges accelerated the cytoskeleton reorganization of osteoblast-like cells. The dielectric properties of polarized HA materials have been examined by Takeda et al. [28] who presented polarization-field (P–E) loops at room temperature. The P–E loops are unlikely to be ferroelectric in origin since the space group of HA is $P6_3/m$ which is non-ferroelectric [29]; although simulations have predicted an anti-ferroelectric to ferroelectric phase transition at ~500 K [30]. The study of polarized porous HA materials is relatively limited [26].

1.1. Conductivity mechanism in HA

The overall mechanism of conduction in HA remains unclear, with the proposed conducting species being ions, namely protons (H^+), oxide ions (O^{2-}) or the lattice hydroxyl ions (OH^-) [7]. The Ca^{2+} [31] and (PO_4^{3-}) [32] ions are not thought to contribute to the conductivity. Khalil et al. [16] proposed that electrical conduction occurred via OH^- migration in the centre of the Ca^{2+} triangle along the *c*-axis. EMF and electrolysis measurements also indicated that OH^- ions are charge carriers [32], although Yamashita et al. [7] questioned the validity of testing pressed (non-sintered) powders. Conduction of protons has been proposed which are transported along OH^- chains [7] and proton conduction has gained favour due to the humidity sensor characteristic of HA. Laghizizil et al. [33,34] considered proton conduction between neighbouring OH^- ions via the reaction:

$$OH^- + OH^- \rightarrow O^{2-} + HOH$$

or a proton jump between OH^- via neighbouring (PO_4^{3-}) ions. The distance between adjacent OH^- ions is thought to be too large (0.344 nm) [7,31] and proton interaction with neighbouring (PO_4^{3-}) ions is favoured (0.307 nm). The dehydroxylation and non-stoichometry of HA during heating is also thought to influence conduction since vacancies at the hydroxyl site (□) are formed via, for example, Eq. (1) [7]:

$$Ca_{10}(PO_4)_6(OH)_2 \rightarrow Ca_{10}(PO_4)_6(OH)_{2-2x}O_x(\square)_x + {}_xH_2O(g)\uparrow \quad (1)$$

where $x < 1$.

In some instances both H^+ and OH^- ions are considered as the conductive species. Nagai and Nishino [13] indicated that room temperature conduction was due to migration of H^+ in adsorbed water and OH^- was thought to contribute at elevated temperatures; particularly since the OH^- vacancies formed during dehydration are likely to obstruct H^+ conduction and facilitate OH^- conduction [31].

1.2. Aims of paper

This paper examines the frequency-dependent relative permittivity, AC conductivity and phase angle of HA from room temperature to 1000 °C, along with the determination of activation energies for conduction. Changes in sintering atmosphere (air or water vapour) will be considered to examine the loss of surface-adsorbed water (dehydration) or OH^- ions from HA (dehydroxylation) during sintering [19]. Samples are thermally cycled to examine the influence of adsorbed water on conductivity and permittivity. Since HA-based materials for bone substitute applications often contain tailored porosity to facilitate bone growth [2,4,5], a comparison will be made between dense and porous materials. The information will also be of interest to understand the conduction mechanisms in the material and to optimize conditions for polarization of HA. To date, only a limited electrical characterization of porous ceramics has been undertaken. Nagai and Nishino [13] examined porous HA in a limited temperature range (below 500 °C). El Hammari et al. [35] studied porous HA at room temperature as a function of relative humidity. Hoepfner and Case [10] considered the room temperature dependency of porosity on the dielectric constant (relative permittivity).

2. Materials and methods

2.1. Manufacture of dense HA ceramics

HA ceramics were manufactured from a commercially available HA powder (TCP130, Thermphos UK Ltd.) that has been successfully used in the production of biocompatible ceramics [36,37]. The powder is a precipitated calcium phosphate with a CaO/P_2O_5 weight ratio of 1.30 to achieve the necessary molar ratio of ~1.67 Ca:P for the formation of HA. The powder, as received, is microcrystalline HA with ~0.5% TCP impurity phases. To form dense discs suitable for characterization, the powder was sieved and compacts were uniaxially pressed at 120 MPa with a 15 mm diameter die for 30 s to achieve suitably robust green bodies without the requirement of binders. The ceramic tablets were sintered at 1300 °C for 4 h with a heating and cooling rate of 60 °C h^{-1}. Sintering was either conducted in air or in the presence of water vapour that continuously flowed along a tube furnace by means of a nitrogen carrier gas. The resulting materials were designated as $dense_{(air)}$ and $dense_{(water)}$, respectively. After sintering, the samples were ground flat to dimensions of 13 mm in diameter and 2 mm thick. The dense ceramic specimens were sintered to 90–95% theoretical density as determined by mass and volume measurements of sintered discs. Fig. 1a shows the macrostructure of the samples, indicating the colour change associated with sintering in

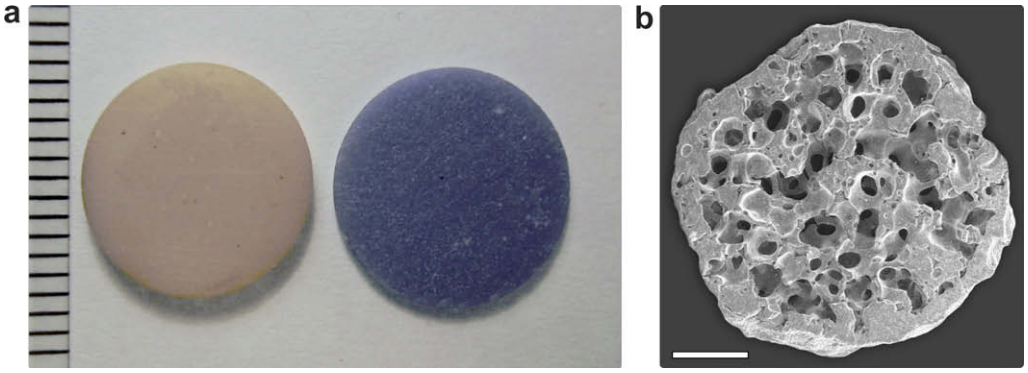

Fig. 1. (a) Optical image of dense discs sintered in water vapour (left) or air (right). Scale bar is in 1 mm divisions. (b) SEM image (low magnification) reveals the structure typical of the highly porous samples prepared. Scale bar is 2 mm.

air (blue) or water vapour (white).[1] The origin of the blue colour after sintering in air is related to the oxidation of impurity manganese ions from Mn^{2+} to Mn^{5+} and the formation of (MnO_4^{3-}) ions at (PO_4^{3-}) sites of HA [38].

2.2. Manufacture of porous HA ceramics

Highly porous HA test pieces were produced via a replication process that utilized polyurethane (PU) foam as a template material, a method that offers a simple route for bioceramics suitable for synthetic bone applications [36,37]. The ceramic slurry was prepared in batches using the same HA powder as the dense materials, incorporated into reagent-grade distilled water with binders, plasticisers and surfactants (polyvinylpyrrolidone, polyvinylalcohol and Dispex A40, respectively) in order to avoid agglomeration and provide a slip with the desired rheology. Once formed the slip was ball milled with zirconia milling media for 24 h at 20 rpm. Commercial PU foams (Sydney Heath and Sons Ltd.) were used as a structural template for the manufacture of CaP bioceramics. The untreated PU foams were graded as 45 pores inch (17.7 pores cm^{-1}), leading to a mean pore size of 564 μm. The thixotropic slurry was incorporated into the PU foam samples with the aid of a mechanical plunging device that ensured the slip coated the walls of the foam. The sample was held above the slip bath to allow the slip to flow and coat the struts of the foam. The samples were dried on tissue paper and treated with high-velocity compressed air to ensure the interconnectivity of the porosity network. Drying of the final samples was carried out at 120 °C for 15 h, followed by sintering in water vapour at 1300 °C in order to produce HA bioceramics with interconnected porosity. Typical sample dimensions were ~9 mm in diameter and ~16 mm in height.

Samples were then cut to a thickness of 2 mm with a diamond-coated wire saw using acetone as a cutting lubricant. The resulting highly porous discs were designated as $porous_{(water)}$ samples. The final porosity level was 60–70 vol.%, measured by optimas image analysis software. Fig. 1b shows the macro porous structure typical of the specimens prepared by this method, which is highly suited to biomedical applications [36].

2.3. Material characterization

For the HA bioceramics prepared, the influence of porosity and sintering atmosphere on phase composition, microstructure and electrical properties were investigated. To assess the effect of sintering atmosphere on the composition of the materials studied, samples were prepared from the air and water vapour sintered tablets, suitable for X-ray powder diffraction (XRD). The materials were ground to a fine powder using a pestle and mortar in ethanol for 5 min, and subsequently dried at 80 °C for 24 h in an oven containing silica bead desiccant. XRD was performed on the two powders using a Phillips diffractometer (PW1710) fitted with a 4 kW X-ray generator, copper target and a graphite monochromator. Control of the diffractometer was achieved using diffraction software PW1877 PC-APD v. 3.5b (October 1999). To assess the phases present, a wide-angle scan was performed, with a 2θ range of 10°–80° sampled at steps of 0.02° with 2 s counting time per step (0.6° min^{-1}). The data collected was analyzed and enhanced (X'Pert Plus, v. 1.0, Philips Analytical), for peak identification and refinement of the unit cell parameters for the phases present. Phases were identified by comparison of peak locations to ICDD reference spectra (HA: 09-0432, α-TCP: 09-0348, β-TCP: 09-0169). Preliminary phase quantification (without internal standards) was conducted using Rietveld refinement (FullProf Suite 2k, v. 3.70) [39] based on the method developed by Reid and Hendry [40].

In addition to establishing the composition of the samples, the microstructure was examined and the grain size determined. A sample of each material was mounted for scanning electron microscopy (SEM) inspection by vacuum impregnation with a low-viscosity epoxy (Struers, Specifix-40). After 24 h curing at ambient, the materials were polished. It was found that extended use of waxed silicon carbide paper for polishing (as opposed to diamond-based

[1] For interpretation of the references to color in this figure, the reader is referred to the web version of this paper.

media) was necessary to minimize grain pull-out due to the low hardness of the HA materials. The samples were ground until planar and polished to ~8 μm with waxed SiC paper and finished with 0.05 μm alumina media on a napless polishing cloth. Etching was performed to reveal grain boundaries, using an 8% solution of phosphoric acid in which the materials were agitated for 10 s and cleaned with distilled water and then ethanol before drying. The samples were gold sputtered before imaging by SEM (JEOL JSM-6310). Digital micrographs were recorded and image analysis performed (ImageJ, v. 1.32, NIH) [41] to determine grain size. Grain size was measured by a linear intercept method due to the efficiency with which large areas can be surveyed, ensuring that in excess of 500 grains were sampled per material.

2.4. Impedance analysis

Permittivity, AC conductivity and phase angle were calculated from complex impedance measured in a frequency (f) range of 0.1 Hz–1 MHz using a Solartron 1260 Impedance analyzer and a 1296 Dielectric Interface. Based on preliminary testing, samples were tested from room temperature to 1000 °C at 50 °C intervals using a voltage of 0.1 V_{rms} (Cycle 1). A heating rate of 1 °C min^{-1} was used with a dwell of 20 min at each measurement temperature. In some cases the temperature interval was reduced to 25 °C to provide additional data to determine the activation energy. After testing from room temperature to 1000 °C (Cycle 1) the sample was subsequently cooled to 125 °C and measurements repeated during reheating of the sample to 1000 °C (Cycle 2). This was undertaken to examine the influence of adsorbed water on conductivity and permittivity.

The AC conductivity (admittance) was calculated using the following equation:

$$\sigma = \frac{Z'}{Z'^2 + Z''^2} \cdot \frac{t}{A}, \tag{2}$$

where Z' and Z'' are the real and imaginary parts of the impedance, A is the area of the sample and t is the sample thickness. The real part of the permittivity was calculated using the following equation:

$$\varepsilon = -\frac{Z''}{Z'^2 + Z''^2} \cdot \frac{t}{\omega . A}, \tag{3}$$

where ω is the angular frequency ($2\pi f$).The phase angle (θ) between current and voltage was determined from the following equation:

$$\theta = \tan^{-1}(Z''/Z'). \tag{4}$$

3. Results and discussion

3.1. Material characterization

The XRD profiles for the samples sintered in either air or water vapour are presented in Fig. 2. All reflections can be accounted for using the reference spectra for HA, β-TCP and α-TCP, with no other significant phases present. Zhou et al. [42] observed that HA loses OH groups when sintered above 1200 °C. Sintering in water vapour suppresses the conversion of α-TCP from the formed β-TCP, but this transformation occurs in the air-sintered material. From the full profile fitting [41] of the materials, the HA unit cell and phases present were quantified (Table 1). The determined unit cell parameters are sufficiently close to those of the standard material (09–0432), a: 10.429 Å, c: 9.418 Å. The phase composition indicates that the majority of the material (~75%) remains as HA, with the remainder composed of TCP phases. In the case of air sintering, α-TCP is the major phase (16%); however, α-TCP is suppressed in the water vapour sintered material and β-TCP is dominant (20%).

The influence of sintering atmosphere was found also to affect the resulting microstructure, as shown in Fig. 3. The voids in Fig. 3 are due to grain pull-out during polishing

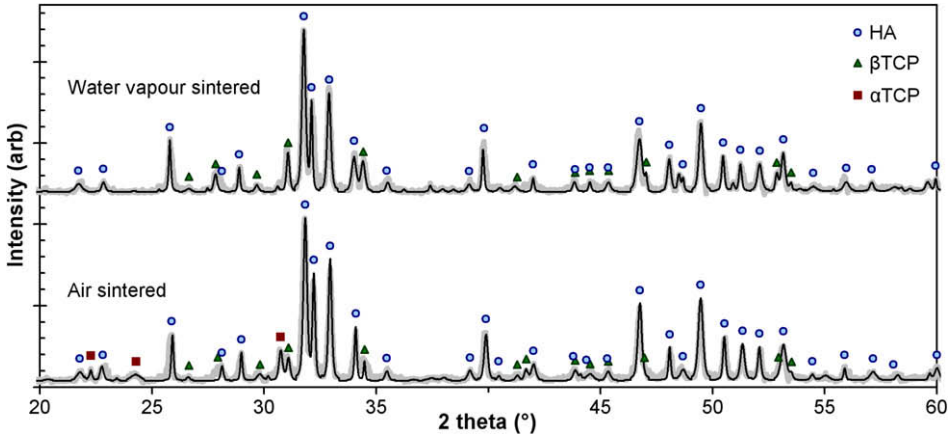

Fig. 2. XRD spectra for dense samples sintered in either air or water vapour. Both materials are principally composed of HA with β-TCP, and in the absence of water vapour α-TCP is formed for the air-sintered material.

Table 1
Activation energies of HA-based materials

Activation energy (eV)	Temperature (°C)	Comments	Ref.
1.86–2.23	700–1000	–	This work
1.5(O^{2-})–2.1(OH^-)	–	Calculated for O^{2-} and OH^-	[55]
3.25–4.90	25–800	HA and TCP	[54]
0.7–1.4	600–800	Ageing phenomena observed	[7]
1.4	600–800	–	[56]
1.21	200–800	–	[33,34]
1.17	600–900	–	[9]
0.9	25–350	–	[16]
0.69	200–800	Pressed powder	[32]
0.08–0.3	200–500	Porous and dense	[13]

rather than inherent microporosity. For the air-sintered material an average grain size of 3.7 μm was measured (Fig. 3a), whereas the dense and porous materials sintered in water vapour had smaller average grain sizes of 2.3 and 2.4 μm, respectively (Fig. 3b and c). However, the microstructure of all three materials may be considered sufficiently similar that it is permissible to compare the electrical properties on an equal basis.

3.2. Electrical properties during the first heating (Cycle 1)

Figs. 4a–6 a show the variation in the real part of the AC conductivity (σ) as a function of frequency for the three HA materials during Cycle 1. Data for only 100 °C intervals are shown for clarity. At low frequencies (<10 Hz) there is little or no frequency dependency of AC conductivity for many of the temperatures tested, particularly at elevated temperatures (>400 °C). For higher frequencies (>10^3 Hz) the AC conductivity rises almost linearly with frequency for all temperatures, following "universal" power law behaviour [43], such that:

$$\sigma(\omega) = \sigma(0) + A\omega^n, \quad (5)$$

where ω is angular frequency, n is a constant ($0 < n < 1$) and $\sigma(0)$ is the low-frequency conductivity. It has been shown [44–46] that this type of frequency response is typical of a resistor–capacitor (R–C) model in which ions in a material are considered as a complex network of conductive (R) and capacitative (C) sites. The conductivity of a conductive site is independent of frequency (analogous to a resistor, since $\sigma = 1R$), while the AC conductivity of a capacitative site rises linearly with frequency (analogous to a capacitor, since $\sigma_{ac} = 2\pi fC$). For HA, the conductive sites can be considered as the channels along which ions are able to move by thermally activated hopping (such as the columnar OH^- ions or protons) and the capacitative sites are ions that are immobile. At low frequencies (<10 Hz) the HA conductivity is governed by the conductive channels (since $2\pi fC$ is low) and the conductivity is frequency independent. Fig. 7 shows the phase angle (θ) as a function of frequency for the porous$_{(water)}$ sample at a variety of temperatures, which is typical for all the materials tested. At frequencies below 10^3 Hz the phase angle approaches 0°, particularly for the materials at high temperature with high conductivity. The low phase angle indicates that current and voltage are in phase and that the material is behaving as a pure conductor. As the frequency is increased, the AC conductivity of the capacitative regions ($2\pi fC$) becomes increasingly significant and Fig. 7 shows that above 10^3 Hz the phase angle approaches −90° since the capacitative regions are now contributing to the overall electrical response.

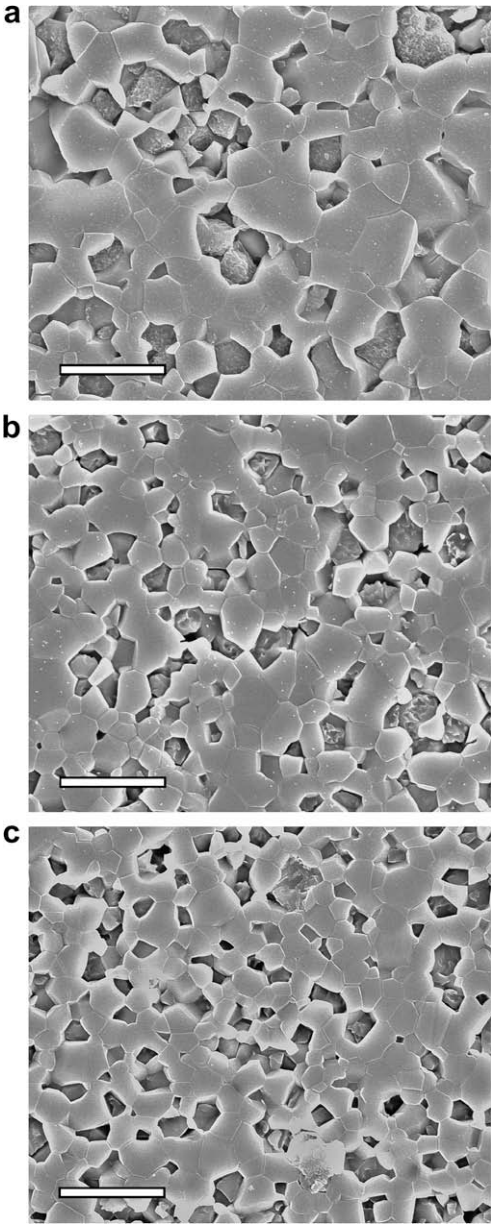

Fig. 3. SEM micrographs of the three materials studied: (a) dense$_{(air)}$, (b) dense$_{(water)}$ and (c) porous$_{(water)}$. Grain size was determined as 3.7, 2.3 and 2.4 μm, respectively (scale bar is 10 μm). The many voids seen are due to grain pull-out during polishing rather than inherent microporosity.

At relatively low temperatures (room temperature to 300 °C) there is an initial decrease in AC conductivity with increasing temperature, particularly for the porous material (Fig. 6a). Roy et al. [47] observed that the HA conductivity decreased when heating from room temperature to 650 °C, a finding that was thought to be related to the loss of bound water. Nagai and Nishino [13] examined released water from HA and proposed that the liberation of water up to 300 °C was related to weakly and strongly physisorbed water. Continued water loss at 500–1000 °C was thought to be due to dehydroxylation of the OH^- lattice (Eq. (1)). As the temperature rises above 300 °C an increase in AC conductivity with increasing temperature is observed (Fig. 6a), in particular in the region of the low-frequency (<10 Hz) plateau which is strongly related to the conductivity of the conductive channels. This is a common occurrence in all the samples irrespective of atmosphere used during sintering of the HA.

Figs. 4a–6a show the variation in the real part of relative permittivity as a function of frequency for a variety of temperatures. All the materials exhibit a frequency-dependent permittivity at all temperatures, with the real part of permittivity decreasing with increasing frequency. This frequency dispersion in HA has been observed by a number of authors [8,11,12,16,17,21,29,30,48,49] and in monoclinic HA [50]. Mahabole et al. [8] stated that the dipole moment

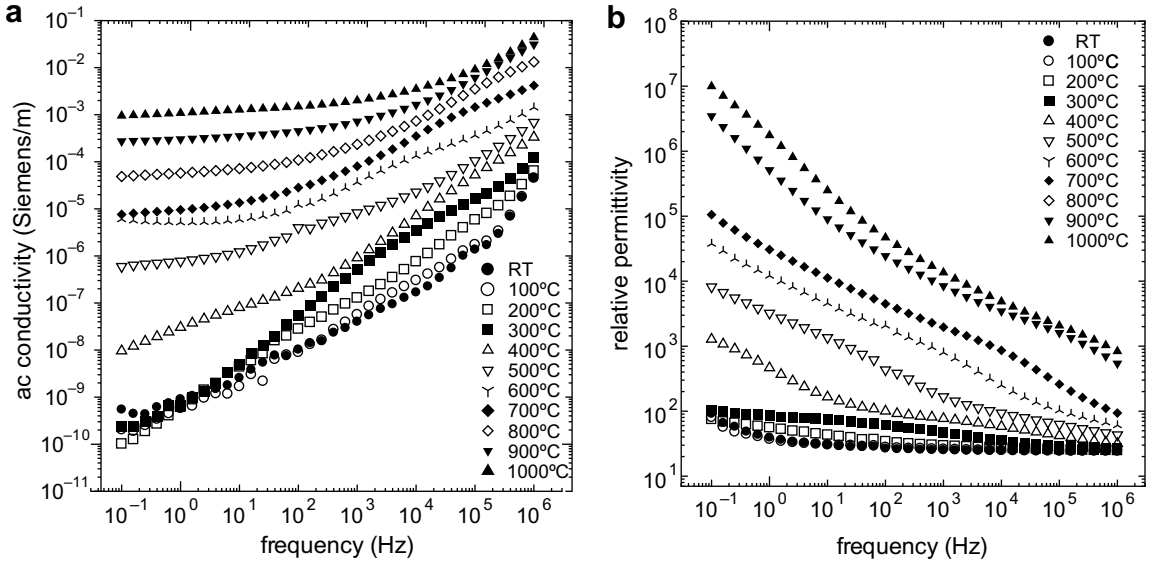

Fig. 4. (a) Real part of AC conductivity for dense$_{(water)}$. (b) Relative permittivity for dense$_{(water)}$.

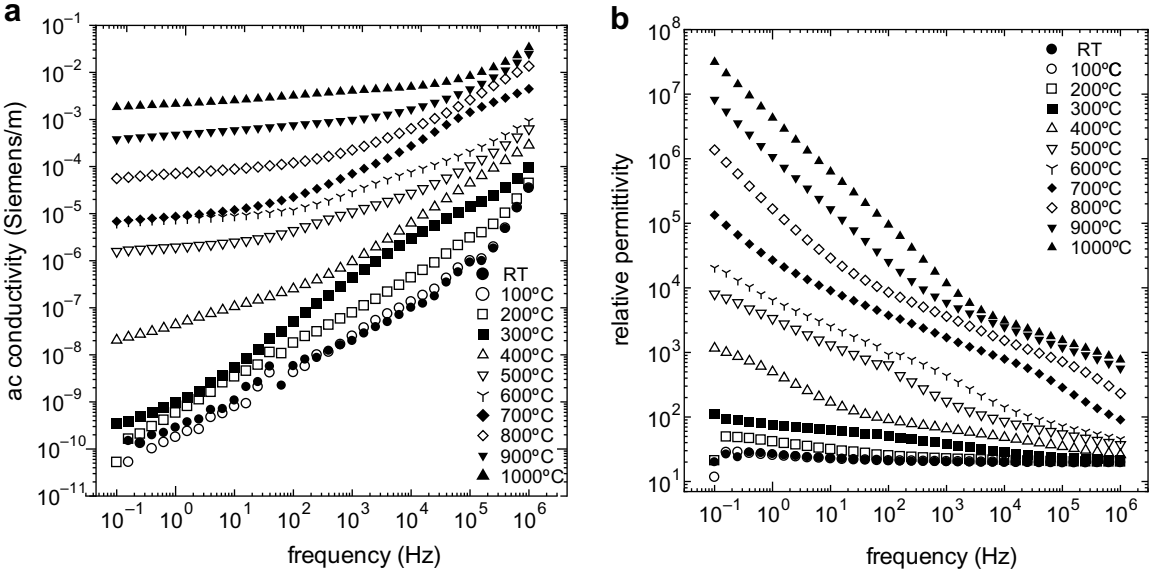

Fig. 5. (a) Real part of AC conductivity for dense$_{(air)}$. (b) Relative permittivity as a function of frequency for dense$_{(air)}$.

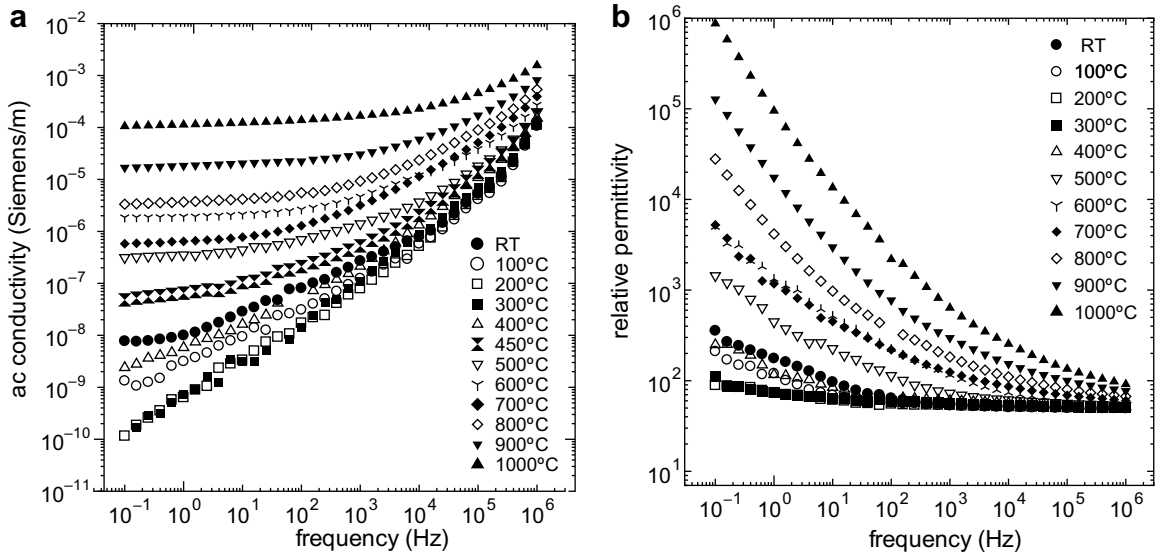

Fig. 6. (a) Real part of AC conductivity for porous$_{(water)}$ for Cycle 1. (b) Relative permittivity for porous$_{(water)}$ for Cycle 1.

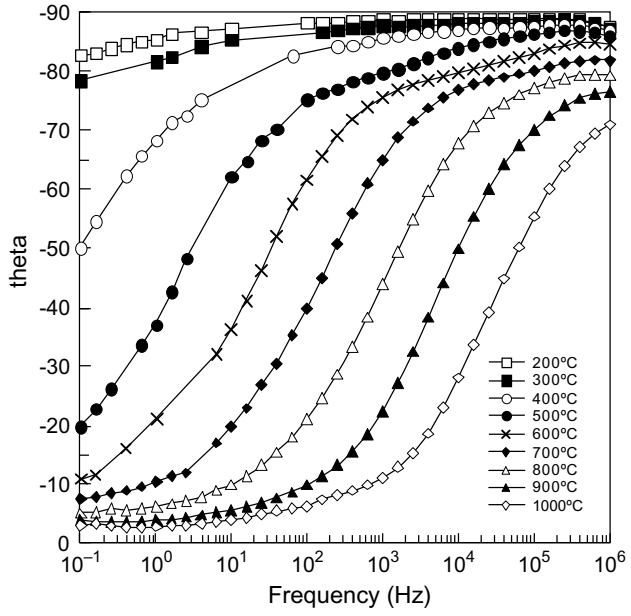

Fig. 7. Phase angle (θ) for porous$_{(water)}$. A phase angle of 0° implies conductive behaviour; a phase angle of −90° implies capacitative behaviour.

of the OH^- ions is a major contributor, although the presence of conductivity in a material can also lead to enhancement in the magnitude of the permittivity and a frequency dependence of permittivity. For example, an increase in the permittivity magnitude and frequency dispersion in ionically conducting zirconia has been observed with increasing temperature [44]. For the porous$_{(water)}$ material the permittivity (Fig. 6b) initially decreases with increasing temperature between room temperature and 300 °C (as observed for the AC conductivity measurements) and indicates that the frequency dispersion is likely to be influenced by the presence of conductivity in the material. Above 300 °C the permittivity begins to rise with increasing temperature for all three materials. Zakarov [11,12] stated that dielectric properties at elevated temperatures are determined by polarization of the "migration type", i.e. the formation of mobile thermal defects. Roy et al. [47] also observed an increase in permittivity with humidity level due to enhanced level of proton conduction.

Fig. 8 shows the low-frequency (1 Hz) dependency of conductivity vs. temperature. An initial decrease in conductivity with increasing temperature from room temperature to ~200 °C can be observed, possibly due to the loss of surface-bound water. Rootare et and Craig [51] studied the vapour-phase adsorption of water on HA, and found that the chemisorbed water monolayer in direct contact with the HA surface was more strongly bound than the additional 1–2 physisorbed water layers [52] that involved only

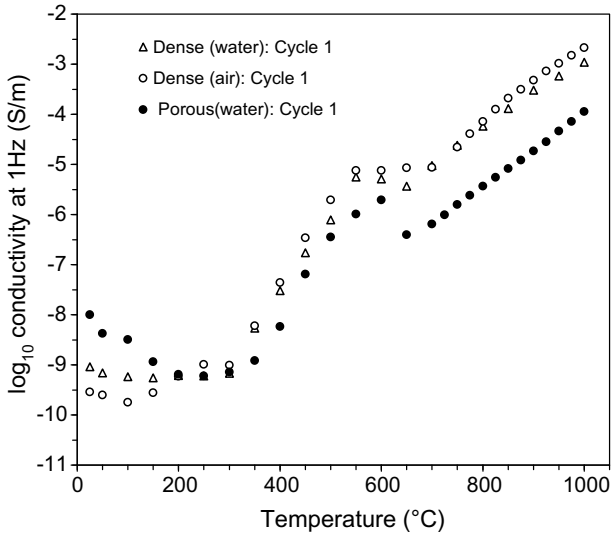

Fig. 8. $\log_{10}$ conductivity vs. temperature for all samples for Cycle 1.

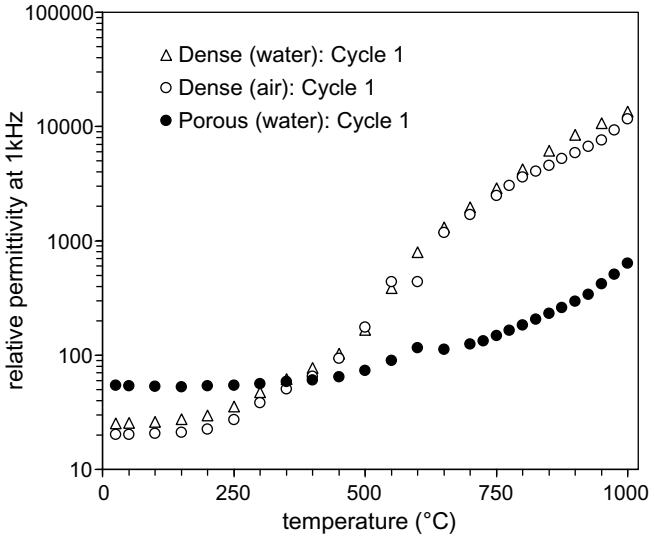

Fig. 9. Relative permittivity at 1 kHz as a function of temperature for Cycle 1.

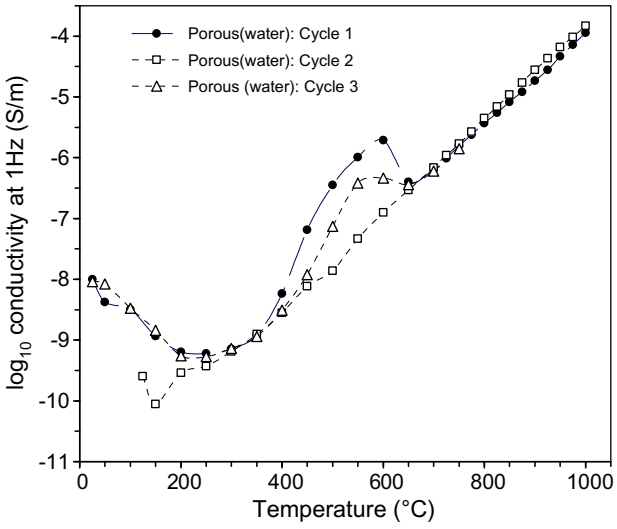

Fig. 11. log conductivity vs. temperature for HA porous$_{(water)}$ for Cycles 1–3.

water–water contacts. Heating at 300 °C in vacuum was necessary to remove the chemisorbed monolayer, whereas the physisorbed layers could be removed at 20 °C in vacuum [51]. Markovic et al. [52] reported thermogravimetry (TG) data for HA. The TG data showed a mass loss of 0.4 wt.% from 30 to 100 °C and 0.3 wt.% from 100 to 250 °C. The total loss on heating to 250 °C corresponded to ~1.5 water layers on the surface of HA, which is thought to be mainly physisorbed water and some chemisorbed water. Between 250 and 360 °C a loss of 0.55 wt.% corresponded to 1 layer of chemisorbed water. The mass fraction lost in the temperature range from 360 to 850 °C was 0.45 wt.% due to dehydroxylation, decomposition and loss of more strongly bound water [51]. It has been reported that the adsorbed water layer can lead to conduction paths which take place by means of a Grotthuss chain reaction [53] in which protons are transferred from one water molecule to the next on the ceramic surface. The water is present due to the attraction between surface hydroxyl groups and water molecules [53]. Comparing the conductivity of all the samples in the temperature range of room temperature to 200 °C, the porous material has the highest conductivity, possibly due to its greater surface area and adsorbed water. The dense$_{(air)}$ sample exhibited the lowest conductivity.

Fig. 8 shows that at 500–600 °C there is a small peak of conductivity for all three materials followed by a continued rise in conductivity at higher temperatures (700–1000 °C). While the porous material has the highest conductivity at low temperatures, the dense samples exhibit higher conduc-

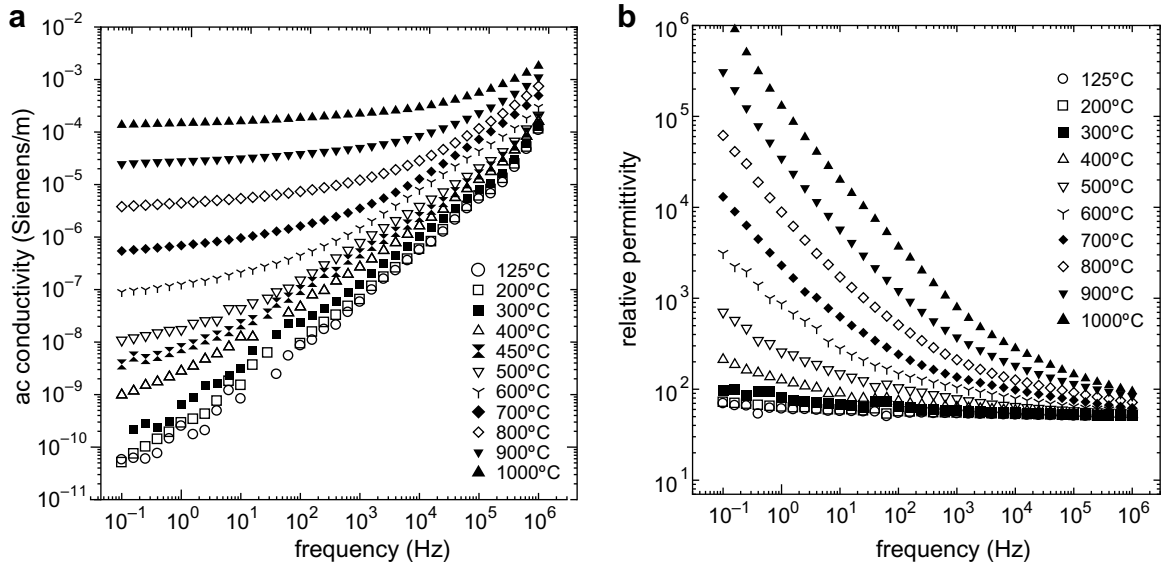

Fig. 10. (a) Real part of AC conductivity for porous$_{(water)}$ for Cycle 2. (b) Relative permittivity for porous$_{(water)}$ for Cycle 2.

tivities at the higher temperatures (700–1000 °C). This is probably due to bulk ionic conduction (rather than surface conduction) being dominant in this temperature range. Nagai and Nishino [13] reported similar conductivity values for the room temperature conductivity, which was higher in a 50 vol.% porous sample (180×10^{-10} S m^{-1}) than a dense material (6.6×10^{-10} S m^{-1}). The conductivity of the dense material was higher than that of the porous material at higher temperatures (500 °C) [13].

Fig. 9 shows the relative permittivity at 1 kHz as a function of temperature: below 250 °C the porous$_{(water)}$ sample with a high surface-to-volume ratio and high conductivity exhibits a high permittivity compared to the dense material. The permittivity begins to increase for all materials above 300 °C, as observed for the AC conductivity. Silva et al. demonstrated an increase in relative permittivity with an increase in temperature [17].

3.3. Electrical properties on subsequent heating (Cycle 2)

In order to understand the role of adsorbed water (dehydration) or dehydroxylation on the electrical properties of HA during Cycle 1 the samples were cooled from 1000 to 125 °C and identical electrical measurements taken during reheating to 1000 °C (Cycle 2). The temperature of 125 °C was chosen to ensure that there was no readsorption of water from the atmosphere on the sample after Cycle 1. Fig. 10 shows the frequency-dependent conductivity and permittivity for the porous material. Similar behaviour was also observed for dense materials (not shown). When comparing the Cycle 2 data with the same sample for Cycle 1 (Fig. 5) the main differences are that at the lower temperatures (<300 °C) the conductivity and permittivity are initially lower for Cycle 2. This is can be observed more clearly in Fig. 11 which shows the low-frequency (1 Hz) conductivity of the material during Cycle 2 and compares the data with Cycle 1. For Cycle 2 the conductivity merely increases with increasing temperature with no initial decrease in conductivity or a small peak in conductivity at ~500–600 °C, as was observed during Cycle 1. While the initial conductivity drop for Cycle 1 at temperatures less than 200 °C can be attributed to the loss of surface-bound water, the reason for the peak in conductivity at ~500–600 °C is less clear. Yamashita et al. indicated that dehydroxylation during measurement of electrical conductivity in air led to an increase in conductivity due to an increase in the initial concentration of free protons [7]. The conductivity was thought to then fall as the material becomes substantially dehydroxylated. The same porous sample was held at room temperature for 1 week and retested (Cycle 3) and conductivity data are also shown in Fig. 11. For Cycle 3 the initial decrease in conductivity when heating from room temperature to 200 °C has returned, along with a slightly smaller conductivity peak at ~500–600 °C. This could indicate that both features are possibly due to surface-bound adsorbed water. Finally, HA conductivity is independent of the thermal history at temperatures of 700–1000 °C and similar conductivities can be observed for the material after all three cycles.

3.4. Activation energies for conduction

Fig. 12 shows complex impedance plots of dense HA sintered in air. The bulk conductivity at each temperature is often determined from the high-frequency intersection of the semicircle with the real axis of the complex impedance [9,13,54] plots to distinguish it from interfacial or electrode impedance. No significant difference was observed when calculating the activation energies using the complex impedance plots or using the low-frequency (1 Hz) plateau conductivities in Figs. 4a–6a; as has been observed by other authors [13]. The plateau conductivities were used to produce an Arrhenius plot of the natural log of bulk conductivity against temperature in order to calculate the

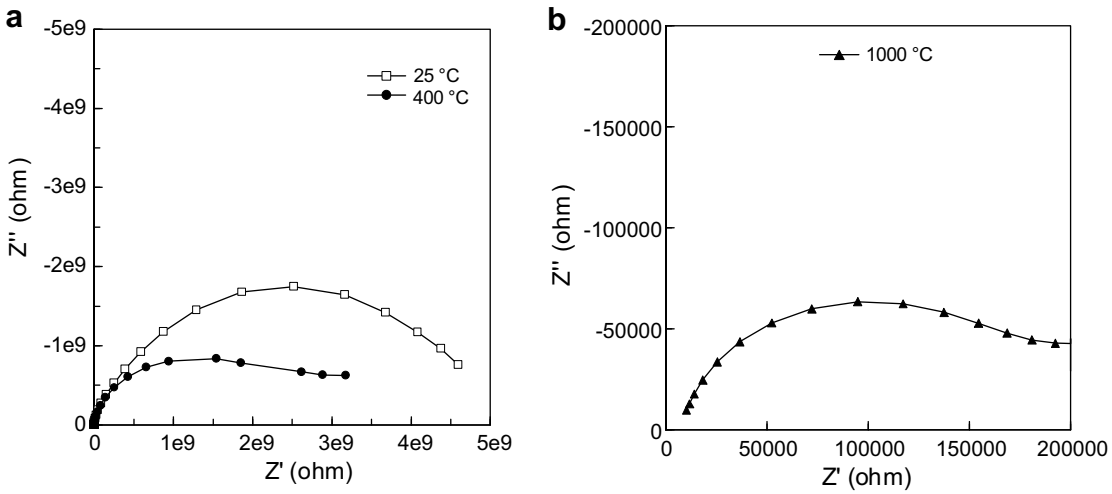

Fig. 12. Complex impedance plots of HA dense$_{(air)}$ at (a) 25 °C and 400 °C, and (b) 1000 °C.

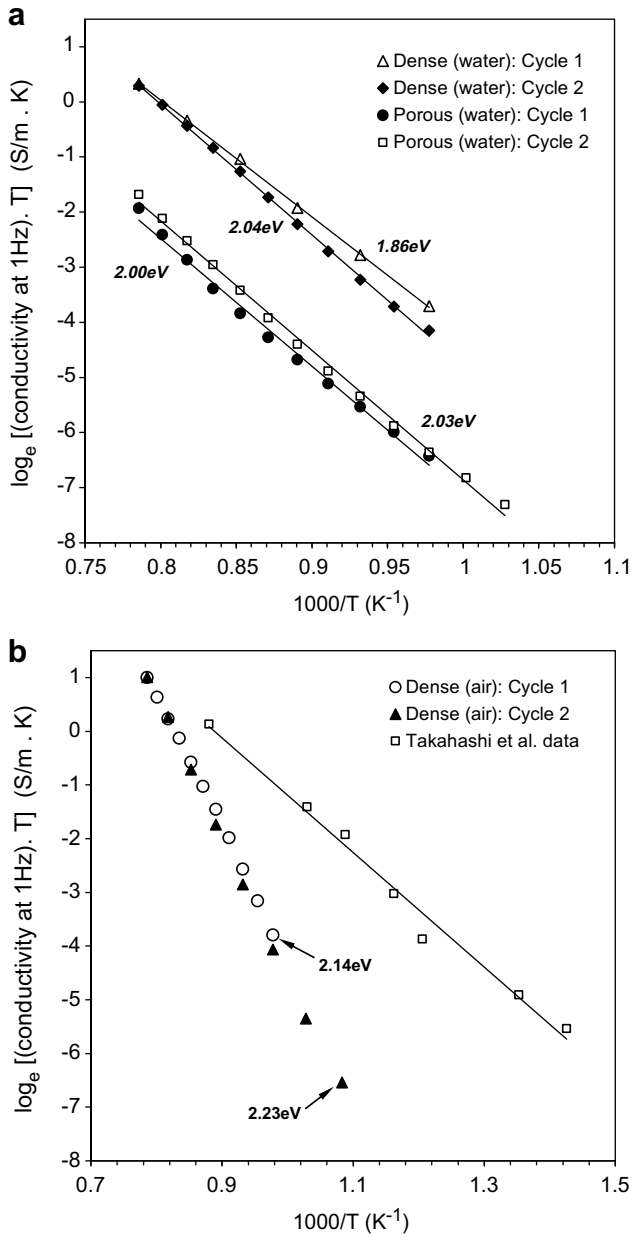

Fig. 13. Arrhenius plot of natural log of bulk conductivity against $1000/T$ (700–1000 °C). (a) $Dense_{(water)}$ and $porous_{(water)}$ and (b) $dense_{(air)}$ with a comparison with data from Takahashi et al. [32] over a similar temperature range.

activation energy for Cycles 1 and 2 for all three materials (Fig. 13). Activation energies could only be determined at high temperatures (700–1000 °C) as only in this region was the temperature dependency of logarithm of conductivity vs. temperature sufficiently linear (see Fig. 8). Since Takahashi et al. [32] published data in a similar temperature range (up to 800 °C) the data is also plotted on Fig. 13b, although, as discussed by Yamashita et al. [7], the measurements were on pressed powders rather than sintered samples. The determined activation energies vary between 1.86 and 2.23 eV. Laghzizil et al. reported an activation energy of 1.21 eV [32,33] and Yamishta reported

Table 2
Cell parameters and phase content determined from full profile XRD fitting, for the air and water vapour sintered materials

Material	HA cell parameters (A)	HA wt%	α-TCP wt%	β-TCP wt%
$Dense_{(air)}$	a: 9.416, c: 6.887	75	16	9
$Dense_{(water)}$	a: 9.422, c: 6.882	76	4	20

0.7–1.4 eV [7]. Table 2 summarizes the published data. Theoretical calculations have determined the activation energy for OH^- ion jumps along the *c*-axis to be 2–2.1 eV [16,55] and for O^{2-} 1.5 eV [55]. The activation for H^+ conduction is much lower (0.5 eV [7]). This indicates that OH^- ions are likely to be responsible for ionic conduction in this high temperature range.

4. Conclusions

This paper has investigated the AC conductivity and permittivity of HA in both dense and porous form and sintered in air or water vapour. At temperatures below 700 °C the permittivity and AC conductivity of HA are influenced by structure and degree of dehydration (thermal history). The AC conductivity exhibited a low-frequency-dependent conductivity followed by a high-frequency-dependent conductivity. The response can be explained in terms of a *R–C* network model consisting of conductive channels in an insulating host medium. The frequency dependence of permittivity and the high permittivity at elevated temperatures is thought to be due to the existence of conductivity in the material. Thermal cycling of the materials indicated that the initial decrease in conductivity with increasing temperatures from room temperature to 200 °C could to be due to dehydration of the HA and loss of surface-bound water. The surface-bound water is thought to contribute to conductivity for both dense and porous materials in this temperature range. The highest conductivity at temperatures <200 °C was exhibited by porous HA sintered in water vapour and was attributed to the large surface area of the materials. Dense materials exhibit the highest conductivities at elevated temperatures (>700 °C) since conduction is dominated by bulk ionic conductivity. The conductivity values are in agreement with those reported by Nagai and Nishino [13] for both porous and dense materials.

Both dense and porous material exhibited a peak in low-frequency conductivity in the range of 500–600 °C which disappeared during Cycle 2 and reappeared during Cycle 3. This indicates that thermal history and degree of surface hydration has an important influence on conductivity in this range. The higher temperature range of 700–1000 °C is unaffected by the thermal cycling and activation energies are in the range of ~2 eV, indicating that OH^- ions are responsible for conductivity at higher temperatures. This information is of interest for (i) understanding the interaction of the HA-based materials with applied electric fields, (ii) the use of electrical measurements for materials charac-

terization; and (iii) the potential use of HA-based materials for sensor applications.

Acknowledgements

The authors show their appreciation and gratitude to the EPSRC (EP/D013798/1) and Great Western Research (HEFCE), UK for their funding of this research.

References

[1] Hench LL. Bioceramics. J Am Ceram Soc 1998;81:1705–28.
[2] Hing KA, Best SM, Tanner KE, Bonfield W, Revell PA. Mediation of bone ingrowth in porous hydroxyapatite bone graft substitutes. J Biomed Mater Res A 2003;68:187–200.
[3] Lee KY, Park M, Kim HM, Lim YJ, Chun HJ, Kim H, et al. Ceramic bioactivity: progresses, challenges and perspectives. Ann Biomed Mater 2006;1:R31–7.
[4] Sopyan I, Mel M, Ramesh S, Khalid KA. Porous hydroxyapatite for artificial bone applications. Sci Technol Adv Mater 2007;8:116–23.
[5] Callcut S, Knowles JC. Correlation between structure and compressive strength in a reticulated glass-reinforced hydroxyapatite foam. J Mater Sci Mater Med 2003;13:485–9.
[6] White AA, Best SM, Kinloch IA. Hydroxyapatite-carbon nanotube composites for biomedical applications: a review. Int J App Ceram Technol 2007;4:1–13.
[7] Yamashita K, Kitagaki K, Umegaki T. Thermal-instability and proton conductivity of ceramic hydroxyapatite at high-temperatures. J Am Ceram Soc 1995;78:1191–7.
[8] Mahabole MP, Aiyer RC, Ramakrishna CV, Sreedhar B, Khairnar RS. Synthesis, characterization and gas sensing property of hydroxyapatite ceramic. Bull Mater Sci 2005;28:535–45.
[9] Yamashita K, Owada H, Umegaki T, Kanazawa T, Futagamu T. Ionic-conduction in apatite solid-solutions. Solid State Ionics 1988;28:660–3.
[10] Hoepfner TP, Case ED. The porosity dependence of the dielectric constant for sintered hydroxyapatite. J Biomed Mater Res 2002;60:643–50.
[11] Orlovskii VP, Zakharov NA, Ivanov AA. Structural transition and dielectric characteristics of high-purity hydroxyapatite. Inorg Mater 1996;32:654–6.
[12] Zakharov NA, Orlovskii VP. Dielectric characteristics of biocompatible Ca-$_{10}$ $(PO_4)_{(6)}(OH)_{(2)}$ ceramics. Tech Phys Lett 2001;27:629–31.
[13] Nagai M, Nishino T. Surface conduction of porous hydroxyapatite ceramics at elevated-temperatures. Solid State Ionics 1988;28–30:1456–61.
[14] Fanovich MA, Castro MS, Porto Lopez JM. Analysis of the microstructural evolution in hydroxyapatite ceramics by electrical characterisation. Ceram Int 1999;25:517–22.
[15] Bowen CR, Gittings J, Turner IG, Baxter F, Chaudhuri JB. Dielectric and piezoelectric properties of hydroxyapatite-$BaTiO_3$ composites. Appl Phys Lett 2006;89:132906.
[16] Sh Kalil M, Beheri HH, Fattah WIA. Structural and electrical properties of zirconia/hydroxyapatite porous composites. Ceram Int 2002;28:451–8.
[17] Silva CC, Graca MPF, Valente MA, Sombra ASB. AC and DC conductivity analysis of hydroxyapatite and titanium calcium phosphate formed by dry ball milling. J Non-Cryst Sol 2006;352:1490–4.
[18] Prieto Valdes JJ, Victorero Rodriguez A, Guevara Carrio J. Dielectric properties and structure of hydroxyapatite ceramics sintered by different conditions. J Mater Res 1995;10:2174–7.
[19] Yamashita K, Kitagaki K, Umegaki T, Kanazawa T. Effect of sintering ambient H_2O vapour on the protonic conduction properties of ceramic hydroxyapatite. J Mater Sci Lett 1991;10:4–6.
[20] Hontsu S, Matsumoto T, Ishii J, Nakamori M, Tabata H, Kawai T. Electrical properties of hydroxyapatite thin films grown by pulsed laser deposition. Thin Solid Films 1997;295:214–7.
[21] Silva CC, Almeida AFL, De Oliveira RS, Pinheiro AG, Goes JC, Sombra ASB. Dielectric permittivity and loss of hydroxyapatite screen-printed thick films. J Mater Sci 2003;38:3713–20.
[22] Itoh S, Nakamura S, Kobayashi T, Shinomiya K, Yamashita K, Itoh S. Effect of electrical polarization of hydroxyapatite ceramics on new bone formation. Calcif Tissue Int 2006;78:133–42.
[23] Nakamura S, Kobayashi T, Yamashita K. Highly orientated calcification in newly formed bones on negatively charged hydroxyapatite electrets. Key Eng Mater 2005;284–286:897–900.
[24] Kim HM, Himeno T, Kokubo T, Nakamura T. Process and kinetics of bonelike apatite formation on sintered hydroxyapatite in a simulated body fluid. Biomaterials 2005;26:4366–73.
[25] Itoh S, Nakamura S, Nakamura M, Shinomiya K, Yamashita K. Enhanced bone ingrowth into hydroxyapatite with interconnected pores by electrical polarization. Biomaterials 2006;27:5572–9.
[26] Yamashita K, Oikawa N, Umegaki T. Acceleration and deceleration of bone-like crystal growth on ceramic hydroxyapatite by electric poling. Chem Mater 1996;8:2697–700.
[27] Nakamura M, Nagai A, Ohashi N, Tanaka Y, Sekilima Y, Nakamura S, et al. Regulation of osteoblast-like cell behaviors on hydroxyapatite by electrical polarisation. Key Eng Mater 2008;361–363:1055–8.
[28] Takeda H, Nakamura S, Yamada K, Tsuchiya T, Yamashita K. Dielectric properties of poled hydroxyapatite ceramics. Key Eng Mater 2000;181–182:35–8.
[29] Silva CC, Valente MA, Grace MPF, Sombra ASB. The modulus formalism used in the dielectric analysis of hydroxyapatite and calcium phosphate with titanium formed by dry ball milling. J Non-Cryst Sol 2005;351:2945–50.
[30] Tofail SAM, Haverty D, Stanton KT, McMonagle JB. Structural order and dielectric behaviour of hydroxyapatite. Ferroelectrics 2005;319:117–23.
[31] Yamashita K, Owada H, Nakagawa H, Umegaki T, Kanazawa T. Trivalent-cation-substituted calcium oxyhydoxyapatite. J Am Ceram Soc 1986;69:590–4.
[32] Takahashi T, Tanase S, Yamamoto O. Electrical-conductivity of some hydroxyapatites. Electrochim Acta 1978;23:369–73.
[33] Laghzizil A, Elherch N, Bouhaouss A, Lorente G, Coradin T, Livage J. Electrical behaviour of hydroxyapatites $M_{10}(PO_4)_6(OH)_2$ (M = Ca, Pb, Ba). Mater Res Bull 2001;36:953–62.
[34] Laghzizil A, El Herch N, Bouhaouss A, Lorente G, Macquete J. Comparison of electrical properties between fluoroapatite and hydroxyapatite materials. J Sol State Chem 2001;156:57–60.
[35] El Hammari L, Laghzizil A, Barboux P, Saoiabi A, Lahlil K. Crystallinity and fluorine substitution effects on the proton conductivity of porous hydroxyapatites. J Solid State Chem 2004;177:134–8.
[36] Gittings JP, Turner IG, Miles AW. Calcium phosphate open porous scaffold bioceramics. Key Eng Mater 2005;284–286:349–52.
[37] Hsu YH, Turner IG, Miles AW. Mechanical characterization of dense calcium phosphate bioceramics with interconnected porosity. J Mater Sci Mater Med 2007;18:2319–29.
[38] Yubao L, Klein CPAT, Xingdong Z, de Groot K. Relationship between the colour change of hydroxyapatite and the trace element manganese. Biomaterials 1993;14:969–72.
[39] Rodriguez-Carvajal J. Recent advances in magnetic structure determination by neutron powder diffraction. Phys B 1993;192:55–69.
[40] Reid JW, Hendry JA. Rapid, accurate phase quantification of multiphase calcium phosphate materials using Rietveld refinement. J Appl Cryst 2006;39:536–43.
[41] Abramoff MD, Magelhaes PJ, Ram SJ. Image processing with ImageJ. Biophotonics Int 2004;11:36–42.
[42] Zhou J, Zhang X, Chen J, Zeng S, De Groot K. High temperature characteristics of synthetic hydroxyapatite. J Mater Sci Mater Med 1993;4:83–5.

[43] Jonscher AK. The "universal" dielectric response. Nature 1977;267:673–9.
[44] Vainas B, Almond DP, Luo J, Stevens R. An evaluation of random *R–C* networks for modelling the bulk ac electrical response of ionic conductors. Solid State Ionics 1999;126:65–80.
[45] Almond DP, Vainas B. The dielectric properties of random *R–C* networks as an explanation of the "universal" power law dielectric response of solids. J Phys Cond Matter 1999;11:9081–93.
[46] Bowen CR, Almond DP. Modelling the "universal" dielectric response in heterogeneous materials using microstructural electrical networks. Mater Sci Tech 2006;22:719–24.
[47] Roy PK, Kalia V, Bera J. Comparison of electrical properties between Ca and Sr hydroxyapatite materials. In: International symposium on advanced materials and processing ISAMAP2K4, 6–8 December 2004, IIT, Kharagpur, India.
[48] Silva CC, Graça MPF, Valente MA, Góes JC, Sombra ASB. Microwave preparation, structure and electrical properties of calcium–sodium–phosphate biosystem. J Non-Cryst Sol 2006;352:3512–7.
[49] Gittings JP, Bowen CR, Turner IG, Baxter F, Chaudhuri J. Characterisation of ferroelectric-calcium phosphate composites and ceramics. J Eur Ceram Soc 2007;27:4187–90.
[50] Ikoma T, Yamazaki A, Nakamura S, Akao M. Preparation and dielectric property of sintered monoclinic hydroxyapatite. J Mater Sci Lett 1999;18:1225–8.
[51] Rootare HM, Craig RG. Vapor phase adsorption of water on hydroxyapatite. J Dent Res 1977;56:1437–88.
[52] Markovic M, Fowler BO, Tung MS. Preparation and comprehensive characterisation of a calcium hydroxyapatite reference material. J Res Natl Inst Stand Technol 2004;109:553–68.
[53] Newnham RE. Electroceramics. Rep Prog Phys 1989;52:123–56.
[54] Nagai M, Shibuya Y, Nishino T, Saeki T, Owada H, Yamashita K, et al. Electrical-conductivity of calcium phosphate ceramics with various Ca/P ratios. J Mater Sci 1991;26:2949–53.
[55] Royce BSH. Field-induced transport mechanisms in hydroxyapatite. Ann N Y Acad Sci 1974;238:131–8.
[56] Owada H, Yamashit K, Umegaki T, Kanazawa T, Nagai M. Electrical properties of apatite ceramics with a microstructure controlled by Y^{3+} substitution. J Ceram Assoc Jpn 1986;94:837–41.